Journal of Power Sources 196 (2011) 8331–8339

Contents lists available at ScienceDirect

Journal of Power Sources

journal homepage: www.elsevier.com/locate/jpowsour

Surface and interface behaviors of $(La_{0.8}Sr_{0.2})_xMnO_3$ air electrode for solid oxide cells

Tongan Jin, Kathy Lu*

Department of Materials Science and Engineering, Virginia Tech, Blacksburg, VA 24061, USA

ARTICLE INFO

Article history:
Received 1 May 2011
Received in revised form 14 June 2011
Accepted 15 June 2011
Available online 22 June 2011

Keywords:
Solid oxide cell
Air electrode
Sr-doped lanthanum manganite
Surface segregation
Interfacial interaction
Chromium deposition

ABSTRACT

In solid oxide cell operation, the stoichiometry of the air electrode is an important factor for its interaction with electrolyte and interconnect and long-term cell performance. In this study, tri-layer samples of yttria stabilized zirconia (YSZ)/$(La_{0.8}Sr_{0.2})_xMnO_3$ (LSM)/AISI 441 stainless steel are made and thermally treated in dry air atmosphere at 800 °C for 500 h. The air electrode composition is varied by changing the x value in $(La_{0.8}Sr_{0.2})_xMnO_3$ from 0.95 to 1.05 (LSM95, LSM100, and LSM105). The LSM composition segregation, YSZ/LSM/AISI 441 interfacial interaction, and the reaction of volatile chromium species with the LSM surface are characterized by scanning electron microscopy (SEM), X-ray photoelectron spectroscopy (XPS), and X-ray diffraction (XRD). Surface segregation of Sr and La are detected for all the LSM samples. Cr deposition is found across the LSM surface. For the LSM95 sample, Sr-containing compound leads to a high Cr content at the YSZ/LSM interface. For the LSM105 sample, on the other hand, the enrichment of La at the YSZ/LSM interface hinders the Cr deposition, leading to a very low Cr content. The mechanisms of LSM elemental surface segregation and Cr deposition are discussed.

1. Introduction

Solid oxide cells (SOCs), including solid oxide fuel cells (SOFCs) and solid oxide electrolyzer cells (SOECs), are promising electrochemical devices in high efficiency electricity generation and novel hydrogen production technologies [1–5]. In order to obtain desired power output or hydrogen production, single cells are connected together by the interconnect. In recent years, lowering the operating temperature of SOCs to 700–900 °C has attracted attention because a reduction in operating temperature means less material degradation such as coarsening of the porous electrodes, stresses and failures caused by mismatches of coefficient of thermal expansion, and sealing problems, and enables replacement of ceramic interconnects by cheaper metallic materials [6,7]. In this temperature range, ferritic alloy (stainless steel) containing 15–25 wt% chromium becomes the choice of interconnect material because it is more cost effective and easier to fabricate [8–12].

However, the degradation of the SOC air electrode has been a challenging problem when the Cr-containing alloy is employed as the interconnect material. This is often caused by Cr-containing species evaporation and transport to the air electrode, which is also called Cr poisoning [13]. Cr poisoning has been observed in both SOFC and SOEC stacks, leading to fast decrease in power output (SOFC) [14,15] or hydrogen production (SOEC) [16,17]. At 700–900 °C, a chromia scale forms on the surface of Cr-containing alloys, which evaporates and forms volatile Cr species. In the oxidizing atmosphere, the volatile Cr species are Cr(VI) compounds and the composition is dependent on the moisture level in the atmosphere. The evaporation occurs as [18]:

$$Cr_2O_3 + (3/2)O_2 \rightarrow 2CrO_3 \quad (1)$$

$$Cr_2O_3 + (3/2)O_2 + 2H_2O \rightarrow 2CrO_2(OH)_2 \quad (2)$$

When the water content is more than 0.1 mol%, $CrO_2(OH)_2$ becomes the dominant volatile Cr species in the atmosphere [18,19].

The volatile Cr species diffuse through the porous air electrode and deposit on the electrolyte/air electrode/air triple phase boundaries (TPB) and the interface of electrolyte and air electrode materials. For different perovskite air electrode materials, Cr poisoning is observed in the widely used strontium-doped lanthanum manganite (LSM) and lanthanum strontium cobaltite ferrite (LSCF) for SOFCs [20,21]. In the SOEC mode, Cr deposition on the LSM oxygen electrode is also believed to cause the degradation of SOEC stacks [17]. However, the mechanism of Cr-containing species interaction with and deposition on the air electrode remains controversial. For the extensively investigated yttria–stabilized zirconia (YSZ)/LSM half cell, the Cr deposition concentrates on the YSZ/LSM interface and blocks the pores of the air electrode under cathodic polarization in the SOFC mode [15,22]. Some studies suggest that the deposition of the Cr species is closely

* Corresponding author. Tel.: +1 540 231 3225; fax: +1 540 231 8919.
E-mail address: klu@vt.edu (K. Lu).

0378-7753/$ – see front matter © 2011 Elsevier B.V. All rights reserved.
doi:10.1016/j.jpowsour.2011.06.052

related to the oxygen activity at the electrode/electrolyte interface (TPB) and competes with the oxygen reduction [15]. In contrast, others believe that the interfacial degradation by Cr poisoning is caused by the blocking of electrochemically active sites by electrochemical reduction of Cr-containing species, which is driven by the thermodynamics without direct influence of the electrical potentials [23,24]. In some further studies, Cr deposition is observed not only at the TPBs, but also in the porous air electrode layer several microns away from the interface [25,26]. Overall, the surface interaction between the LSM air electrode and the volatile Cr species has not been well defined. First, the overall Cr deposition process is complicated, and there are many different parameters, such as temperature, atmosphere, and cell structure, leading to varying results. Second, the Cr species deposition on TPBs, electrolyte, and electrode surface has different but convoluted mechanisms. Third, the Cr species have very low concentrations in both gaseous and solid phases, which make the characterization difficult. The interference of different elements during the characterization also presents problems.

The resulting phases of the Cr species interaction with the LSM air electrode have not been well defined [26]. Although $MnCr_2O_4$ and $(Mn,Cr)_3O_4$ spinel phases as well as Cr_2O_3 have been identified in the LSM air electrode and contact layer [27,28], the surface chemistry of the Cr poisoning and the degradation mechanism of the LSM electrode are not clear. Previous work indicates that Mn is an important factor for the reactions between the volatile Cr species and the LSM electrode [23]. Different LSM stoichiometry such as excessive or deficient Mn can lead to differences in such surface reactions. Detailed study of the interactions of the electrolyte/air electrode/interconnect tri-layer can improve the understanding of the Cr poisoning process and the interaction at the interfaces.

In this work, LSM air electrodes with different stoichiometry ($(La_{0.8}Sr_{0.2})MnO_3$, $(La_{0.8}Sr_{0.2})_{0.95}MnO_3$, and $(La_{0.8}Sr_{0.2})_{1.05}MnO_3$ (LSM100, LSM95, and LSM105)) are prepared on YSZ electrolyte. AISI 441, a stainless steel, is applied on the YSZ/LSM bi-layer as a SOC interconnect material. The tri-layer samples are thermally treated at 800 °C for 500 h. The LSM electrode composition and the Cr distribution in the porous air electrode are analyzed to examine the LSM stoichiometry effect on the Cr deposition and the interface reactions. The phases at the interfaces are determined.

2. Experimental procedures

2.1. Sample preparation

LSM powders with different stoichiometry were prepared with a conventional solid state reaction method [29]. $SrCO_3$ (99.9%, Sigma–Aldrich, St. Louis, MO), La_2O_3 (99.98%, Alfa Aesar, Ward Hill, MA), and $MnCO_3$ (99.9%, Alfa Aesar, Ward Hill, MA) at designed composition ratios (LSM95, LSM100, and LSM105) were mixed in a ball mill overnight. The mixed oxide and carbonates were calcined in a box furnace (DelTech, Model DT-31-Fl-8-C, Denver, CO) at 1200 °C for 20 h. The LSM air electrode was fabricated on the YSZ surface by screen printing [30]. The LSM layer on the YSZ substrate (8 mol% yttria stabilized zirconia, 20 mm diameter, 250–290 μm thickness, NexTech Materials, Lewis Center, OH) was 20–30 μm thick after being sintered at 1100 °C for 2 h.

After the sintering of the YSZ/LSM bi-layer, the AISI 441 alloy was placed on the LSM electrode as the interconnect. The configuration of the YSZ/LSM/AISI 441 tri-layer was given in a previous article [30]. Also, some YSZ/LSM bi-layer samples were prepared without the AISI 441 interconnect layer. All the tri-layer (with AISI 441) and bi-layer (without AISI 441) samples were thermally treated in a tube furnace (1730–20 HT Furnace, CM Furnace Inc. Bloomfield, NJ). The thermal treatment was carried out in dry air (compressed air) at 800 °C for 500 h. The thermal treatment set-up was shown in the previous article [30]. In order to observe the TPB region, the LSM porous layers were peeled off to show the YSZ/LSM interface for the 500 h thermally treated samples.

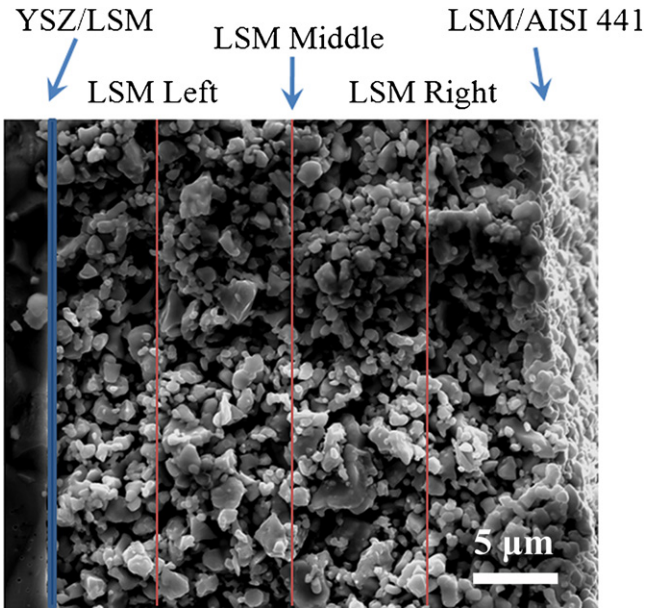

Fig. 1. Examination of the locations of the porous LSM air electrode. XPS is carried out at 5 locations: YSZ/LSM, LSM left, LSM middle, LSM right, and LSM/AISI 441.

2.2. Characterization

After the thermal treatment, the tri-layer samples were broken to examine the cross-sections. Some samples were mounted into epoxy, and then cut and ground to study different positions (distances away from the AISI 441 layer) in the porous LSM air electrode. Along the 30 μm thick LSM layer, the examined locations are shown in Fig. 1. They were labeled as YSZ/LSM, LSM left, LSM middle, LSM right, and LSM/AISI 441 from the YSZ to the AISI 441. To study the microstructure, both secondary electron images and backscattered electron images of scanning electron microscopy (SEM, Quanta 600 FEG, FEI, Hillsboro, OR) were used. Surface analysis was carried out in an X-ray photoelectron spectrometer (XPS, PHI Quantera SXM-03, Physical Electronics Inc., Chanhassen, MN). An Al Kα radiation (1486.6 eV) was used as the X-ray source. In order to identify the phases, X-ray diffraction (XRD) studies were carried out in an X'Pert PRO diffractometer (PANalytical B.V., EA Almelo, The Netherlands). The step size was 0.030° s^{-1} with Cu Kα radiation (λ = 1.5406 Å).

3. Results

3.1. Microstructure

The SEM images of the YSZ electrolyte/LSM air electrode/AISI 441 interconnect cross-sections are shown in Fig. 2. The top images are before the thermal treatment and the bottom images are after that. The images are taken from the polished tri-layer samples mounted in epoxy. The thickness of the LSM porous layer is 25–30 μm. Fig. 2 shows that the tri-layer configuration is maintained. Before the thermal treatment, the LSM grains appear to have been sintered (top of Fig. 2a–c). The porous LSM air electrode layer is homogeneous for all the three different compositions (LSM95, LSM100, and LSM105). The grain size distribution of the LSM electrode increases from LSM95 to LSM105. For the LSM95 sample,

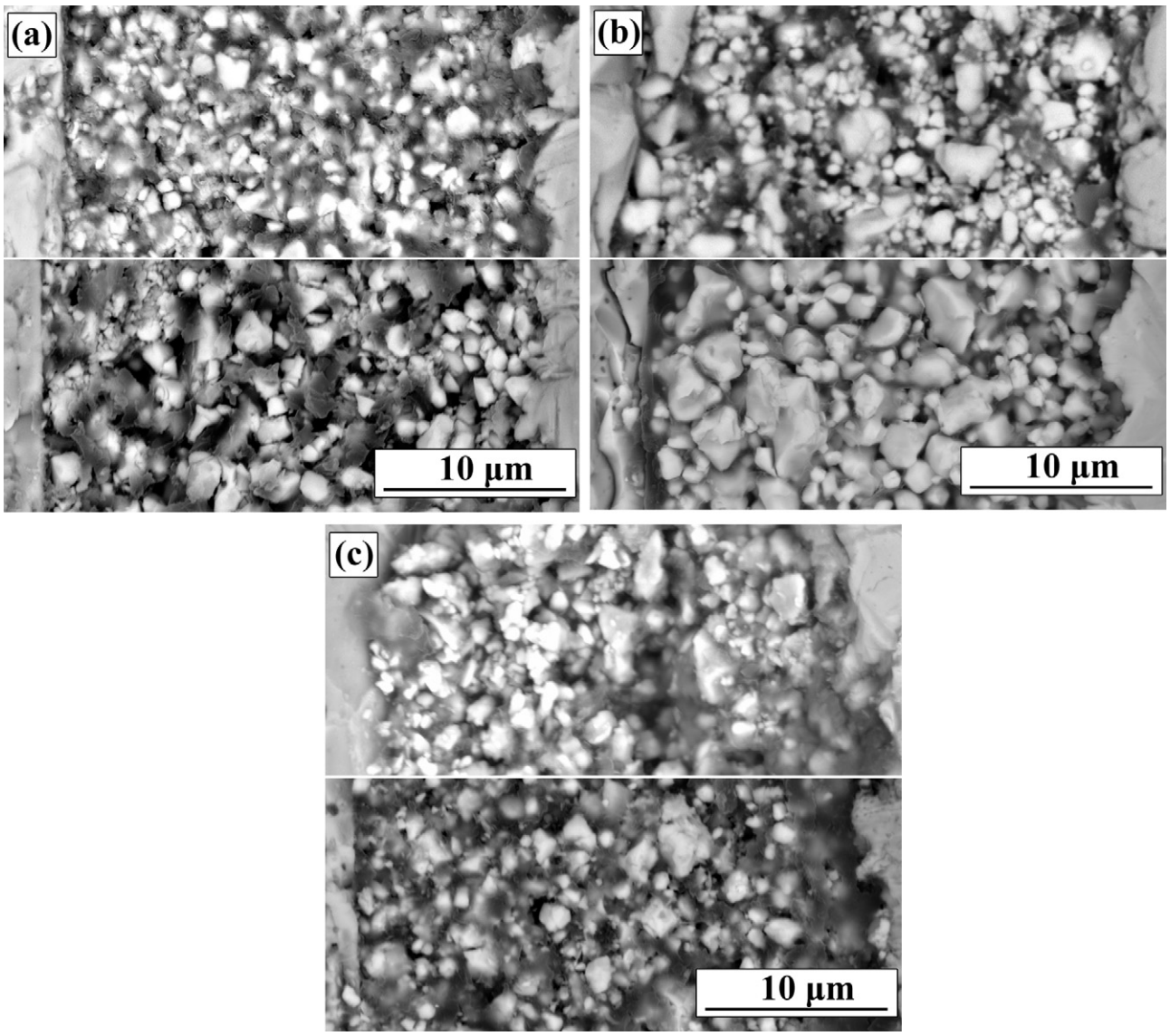

Fig. 2. SEM images of YSZ/LSM/AISI 441 tri-layer cross-sections before and after the thermal treatment in air at 800 °C for 500 h:(a) LSM95, (b) LSM100, and (c) LSM105. For each figure, the top is before the thermal treatment and the bottom is after the thermal treatment. The samples are mounted in epoxy and polished.

the grains are 2–4 μm and almost no small grains below 1 μm can be seen. For the LSM100 and LSM105 samples, smaller grain sizes below 1 μm are apparent and some large grains of ~5 μm are observed. The grain size of the LSM100 sample is slightly larger than that of the LSM105 sample. The LSM95 sample shows the most compact network among the three samples. For the other two samples, local porous regions are more prevalent. Also, the grains in the LSM100 and LSM105 samples do not bond well.

Fig. 3 shows the SEM images of the un-mounted, fractured YSZ/LSM bi-layer cross-sections, before (top) and after (bottom) the thermal treatment. The porous LSM layer can be observed without the possible damage from grinding and polishing. In the SEM images, the YSZ electrolyte is dense although small closed pores are present. Among the three studied samples, all the interfaces show good contact between the YSZ electrolyte and the LSM electrode before the thermal treatment (top of Fig. 3a–c). The LSM grain size difference is consistent with that in Fig. 2. The LSM95 sample has more uniform grain sizes. The LSM100 and LSM105 samples show larger grain size distribution, especially for the LSM100 sample. For the LSM95 sample, the LSM grains and the YSZ surface seem to form better contact. For the LSM100 and LSM105 samples, the contact of the LSM grains with the YSZ surface may be slightly less. These different microstructures indicate that the Mn-excessive sample (LSM95) is easier to be sintered and forms better contact with the YSZ electrolyte.

After the thermal treatment of the tri-layer and bi-layer samples in air at 800 °C for 500 h, the microstructure (bottom of Figs. 2a and 3a) of the LSM95 layer becomes more porous without significant change in the LSM grain size. This is mainly because the sintering process at 1100 °C has consumed the excessive surface energy, the LSM microstructures such as porosity, pore size, and pore structure are mostly determined by the sintering process. The thermal treatment at 800 °C causes only slight morphological change. For the LSM100 sample, however, the microstructure changes after 500 h of thermal treatment are more visible (bottom of Figs. 2b and 3b). Some small LSM grains (<1 μm) disappear and large grains connect and form a continuous network. The grain size is about 2–5 μm after 500 h of thermal treatment. For the LSM105 sample, the microstructure shows the smallest sintered grain sizes (bottom of Figs. 2c and 3c), there is no fundamental grain size

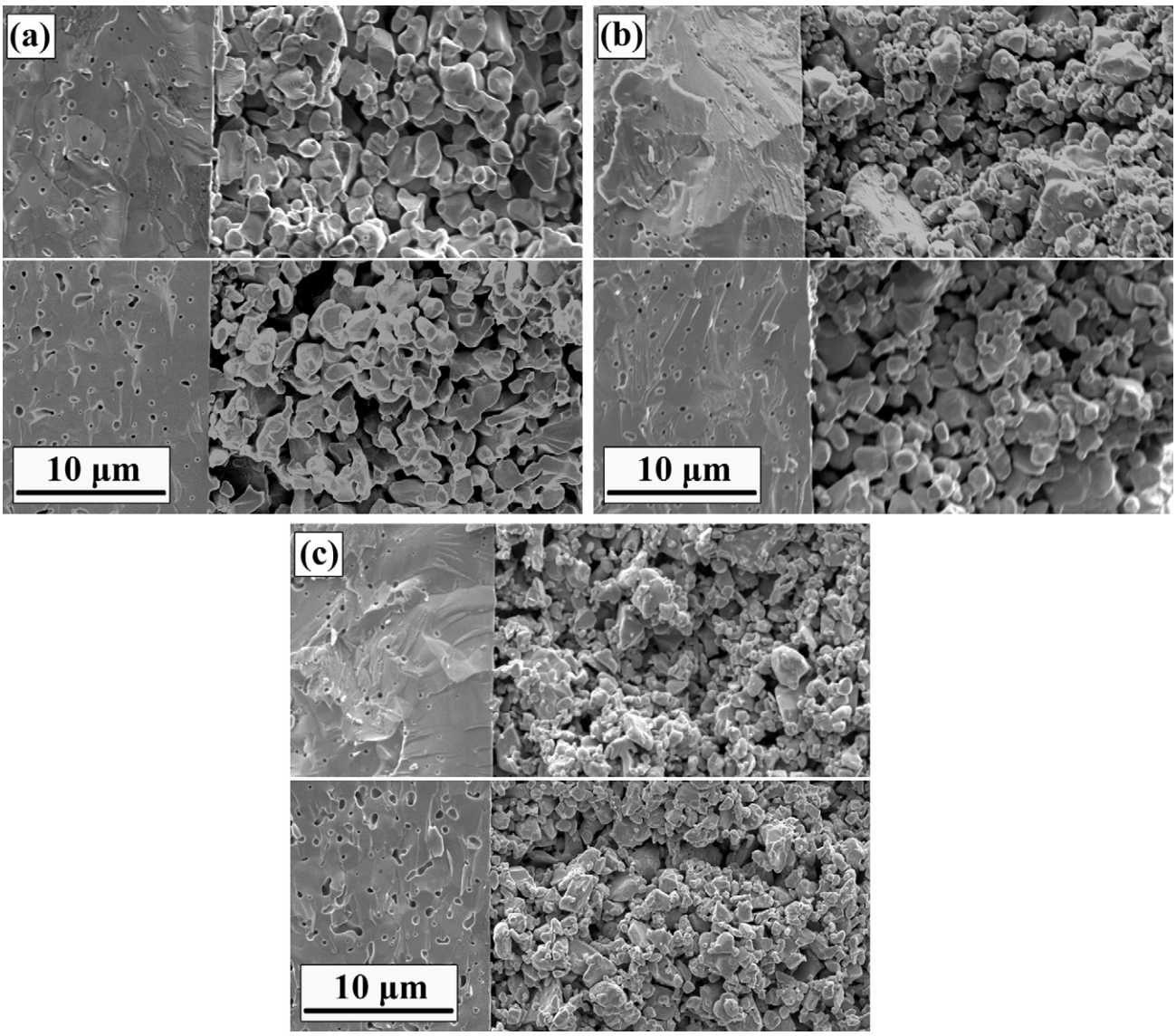

Fig. 3. SEM images of YSZ/LSM bi-layers before and after the thermal treatment in air at 800 °C for 500 h (unpolished cross-section): (a) LSM95, (b) LSM100, and (c) LSM105. For each figure, the top is before the thermal treatment and the bottom is after the thermal treatment.

change after the thermal treatment. For the YSZ/LSM interfaces, after the thermal treatment, the LSM105 sample shows the most contact with the YSZ followed by the LSM100 sample and then the LSM95 sample. However, the bonding between the YSZ and the LSM does not necessarily follow the contact trend, as seen in Section 3.2.

3.2. YSZ/LSM interface analysis

To examine the microstructure at the YSZ/LSM interface, the LSM porous layer was mechanically peeled off from the YSZ substrate and the resulting YSZ surface morphologies are shown in Fig. 4 for different conditions. Fig. 4a is the surface of the YSZ substrate, which shows no change during the sintering and the thermal treatment. The grain boundaries are clearly visible and the grain size is about 5 μm. For the LSM95 sample, the LSM layer forms extensive bonding spots with the YSZ layer even before the thermal treatment (Fig. 4b top). For the LSM100 and LSM105 samples, the bonding with the YSZ diminishes at the as-sintered state (top of Fig. 4c and d). After the thermal treatment, the LSM95 sample still shows extensive bonding with the YSZ; the YSZ surface is almost totally covered with LSM. Fig. 4b bottom shows the low and high magnification images respectively. The YSZ grain boundaries cannot be seen. For the LSM100 and LSM105 samples (Fig. 4c and d) bottoms, also with low and high magnification images), the bonding spots (the round features) with the YSZ surface and the residual LSM (the coverage of the YSZ grains) on the YSZ surface diminish in the same order. For the LSM100 sample, the bonding spots increase compared to the as-sintered state, which means more contacts are formed during the thermal treatment (Fig. 4c). However, the grain boundaries of the YSZ surface are still visible; the high magnification image shows less extensive bonding struts. For the LSM105 sample (Fig. 4d), there are very few bonding spots after the thermal treatment; very little LSM residual is seen on the YSZ surface. The high magnification image clearly reveals the YSZ grain boundaries and very few, weak bonding spots with negligible bonding struts. This trend is different from the interface contact result discussed in Section 3.1. However, it is consistent with the adhesion strength observed between the LSM layer and the YSZ layer for the different samples.

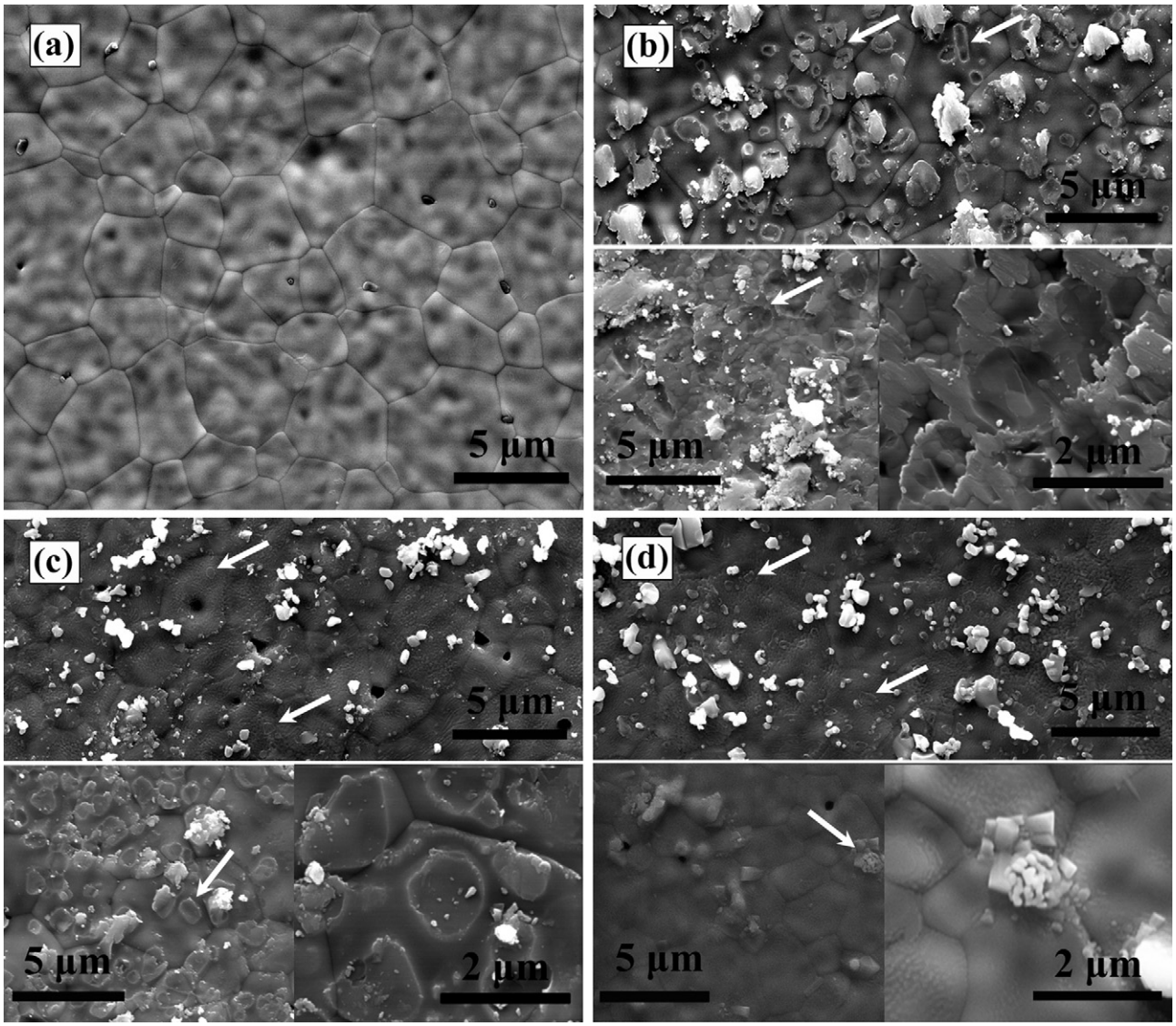

Fig. 4. SEM images of the YSZ/LSM interface after the LSM porous layer removal. (a) YSZ surface, (b) LSM95, (c) LSM100, and (d) LSM105. For (b), (c), and (d), the top is the as-sintered sample and the bottom is the thermally treated sample with low and high magnifications.

3.3. LSM/AISI 441 interfacial composition analysis

In order to examine the LSM layer chemical composition and understand the interfacial interaction between LSM and AISI 441, the AISI 441 interconnect is removed for the XPS analysis. The elemental compositions at the LSM/AISI 441 interface at different conditions are shown in Fig. 5. The scan area is 200 μm × 200 μm. Since the LSM samples are mounted in oxygen-containing epoxy, oxygen is excluded from the analysis. The atomic percentages of La, Sr, Mn, and Cr are normalized to 100%. Each atomic percentage result from the XPS analysis is averaged by three scans, the standard deviations are also shown in Fig. 5.

The initial composition of the LSM samples is shown in Fig. 5 as a reference. After being sintered at 1100 °C for 2 h, the surface compositions of the LSM samples are different from the initial compositions (Fig. 5a). Sr and La show enrichment on the LSM surface. Sr increases by 46% in LSM95, 42% in LSM100, and 23% in LSM105; La increases by 31% in LSM95, 24% in LSM100, and 33% in LSM105. Accordingly, Mn decreases on the LSM surface by 32% in LSM95, 28% in LSM100, and 33% in LSM105. It should be reminded that oxygen is excluded from the analysis and these changes are for the relative change of the respective metal elements only. The surface Sr and La segregation can be understood as follows. The crystal structure of the LSM surface is different from that in the bulk. Broken bonds and strain energy drive composition re-distribution [31,32]. For LSM, Sr surface segregation is a well-known phenomenon [33–37]. La^{3+} (1.36 Å) and Sr^{2+} (1.44 Å) have much larger ionic radii, whereas Mn^{3+}/Mn^{4+}ions are relatively small (less than 1 Å) [38]. As a result, La and Sr are more likely to reside on the surface for size accommodation. Sr shows more surface enrichment than La for the LSM95 and LSM100 samples, which causes the La/Sr ratio to decrease to 3.5 from the initial ratio of 4 (Fig. 5b). For the LSM105 sample, the La/Sr ratio increases to 4.3. This is likely because the excessive A sites of the LSM perovskite structure offer more accommodation to La. In the meantime, Mn content decreases significantly (Fig. 5a), likely because of Mn migration to the LSM bulk due to its small size. The (La + Sr)/Mn ratio thus increases significantly. Initially the (La + Sr)/Mn ratios are 0.95, 1, and 1.05 respectively (Fig. 5c). At the as-sintered state, this ratio increases to 1.8–2.0. The significant change of the AB^{-1} site ratio in the LSM indicates that the LSM surface may not maintain the perovskite crystal structure.

For the YSZ/LSM bi-layers without the presence of the AISI 441 interconnect after the 500 h thermal treatment, the surface compositions of the LSM samples change continuously compared to

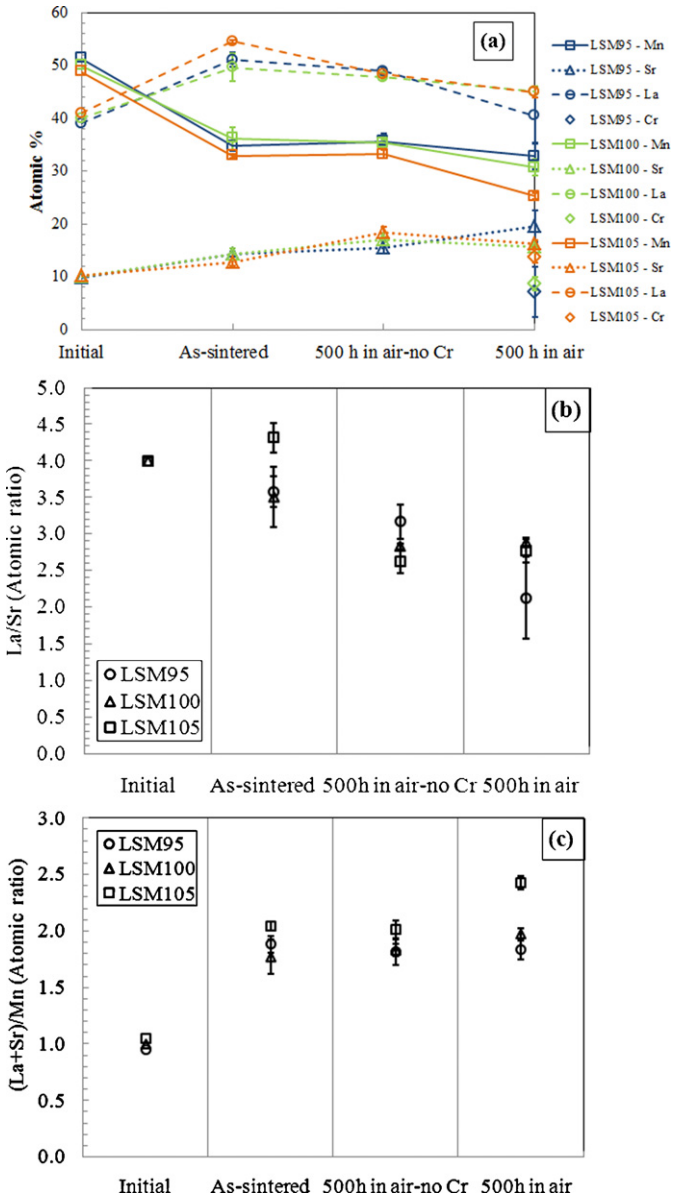

Fig. 5. Elemental concentrations of the LSM samples: (a) atomic concentrations, (b) La/Sr ratio, and (c) (La + Sr)/Mn ratio.

the as-sintered state (Fig. 5a). La decreases by 4% in LSM95 and LSM100, and 11% in LSM105. The surface segregation of Sr continues, increasing by 9% in LSM95, 19% in LSM100, and 46% in LSM105. The La/Sr ratios of LSM95, LSM100, and LSM105 are 3.1, 2.8, and 2.6 respectively (Fig. 5b). These values are drastically lower than the designed value of 4.0. Mn stays almost the same in all the LSM samples, where the Mn contents of the three samples are close to each other at 33–36%. This means that the thermal treatment causes La to migrate inward, even though the extent is less. Mn change is insignificant. Regardless, since La decreases and Sr increases for all the LSM samples, the (La + Sr)/Mn ratios stay similar to those of the as-sintered samples at 1.8–2.0 (Fig. 5c). These values again are very different from the designed value of 0.95–1.05 and indicate likely crystal structure change on the LSM surface.

For the YSZ/LSM/AISI 441 tri-layers, after the thermal treatment for 500 h, Cr is detected on the LSM surface. For the LSM105 sample, the Cr concentration on the surface is 13.7%, which is higher than those of the LSM95 and LSM100 samples at 7.1% and 8.7% respectively (normalized to 100% of La, Sr, Mn, and Cr). If oxygen

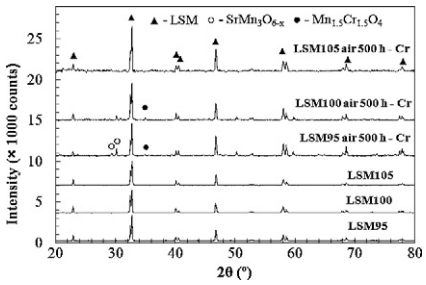

Fig. 6. XRD patterns of the LSM layer before and after the thermal treatment at 800 °C for 500 h in air. The latter case is the tri-layer arrangement.

was included in the atomic percent calculation, the Cr deposition amounts would be 2–5%, much higher than those from the energy dispersive spectroscopy (EDS) analysis [30]. The reason is that XPS collects composition data from at most ~10 nm depth while EDS collects composition data from ~1 μm deep [39]. For the Cr deposition on the LSM surface, XPS surface analysis is a more sensitive technique.

After the tri-layer sample thermal treatment, La decreases for all the three samples compared to the as-sintered samples, by 21% in LSM95, 9% in LSM100, and 17% in LSM105 respectively. At the same time, Mn decreases by 5% in LSM95, 15% in LSM100, and 23% in LSM105; and Sr increases by 37% in LSM95, 10% in LSM100, and 28% in LSM105. Just as for the bi-layer samples, the Sr enrichment and Mn depletion on the surface are also observed. However, La decreases more significantly on the surfaces than for the bi-layer samples. This is believed to result from Cr^{3+} taking the place of La^{3+} in the surface structure and causing La^{3+} to diffuse into the LSM samples. For LSM95, Sr increases by 37% compared to the as-sintered state, which is much higher than the increase for the bi-layer sample (9%). For LSM100 and LSM105, the Sr increases are much less than those of the bi-layers. This is likely because Mn diffuses inward instead of relatively unchanged for the tri-layer samples, which provides more room for Sr to resist segregation. Interestingly, after the tri-layer thermal treatment, the Mn surface concentrations of the LSM95 and LSM100 samples are very close, at 31% and 33% respectively (Fig. 5a), whereas the LSM105 sample shows a lower Mn surface concentration at 25%. Apparently, higher La and Sr contents lead to more Mn segregation. Since the LSM95 sample has more Sr and less La, the La/Sr ratio of the LSM95 sample is 2.1 while those for the LSM100 and LSM105 samples are 2.8 and 2.9 respectively (Fig. 5b). In any case, these values are much lower than the designed ratio of 4.0 and indicate crystal structure instability. The (La + Sr)/Mn ratios of the LSM95 and LSM100 samples are very close to the same value of 1.9 (Fig. 5c) while for the LSM105 sample it is 2.4, still all much higher than 1. For the LSM95 sample, Cr leads to a 15% decrease in La and a slight decrease in Mn, while Sr increases more significantly than that of the no-Cr condition. For the LSM100 sample, both La and Mn decrease and Sr increase are less than those of the no-Cr condition. The final result is similar (La + Sr)/Mn ratios. For the LSM95 and LSM100 samples, Cr likely forms Mn–Cr compounds with Mn. For the LSM105 sample, the Mn content is less than those of the LSM95 and LSM100 samples and the Cr content is significantly higher; this result may be caused by the excessive La and Sr interaction with Cr species, which also increases the amount of Cr surface deposition. However, other analysis such as XRD cannot verify this conjecture.

3.4. LSM/AISI 441 interface phase evolution

XRD patterns of the LSM samples with different stoichiometries (LSM95, LSM100, and LSM105) are shown in Fig. 6. Before the thermal treatment, the LSM95, LSM100, and LSM105 air electrodes

show almost pure perovskite phase. The excessive and deficient Mn contents in the non-stoichiometric samples (LSM95 and LSM105) do not lead to visible phase separation of the LSM samples. After the thermal treatment for 500 h at 800 °C in air and without contact with the AISI 441 interconnect, the XRD patterns of all the three samples show no detectable change (not shown in Fig. 6). The surface segregation detected by the XPS analysis is located only on the very surface, which is beyond the detection limit of the XRD analysis. The bulk phases of the LSM samples with different stoichiometries are stable during the thermal treatment. This also explains why the drastic LSM surface composition segregation has not been widely reported.

For the tri-layer samples, after the thermal treatment at 800 °C for 500 h, the LSM layers with different stoichiometries mainly contain the same perovskite phase. However, some other phases are identified. $SrMn_3O_{6-x}$ is a minor phase identified in the LSM95 sample, which cannot be detected in the other 2 samples. The $SrMn_3O_{6-x}$ phase may correspond to the surface phase of the LSM95 sample with a higher Sr concentration. A minor $Mn_{1.5}Cr_{1.5}O_4$ phase is detected in the LSM95 and LSM100 samples. For the LSM105 sample, no other phase can be identified besides the perovskite LSM. As indicated in Section 3.3, the Cr species may interact with La and Sr and form $(La,Sr)CrO_3$. However, no new phase is detected by XRD because the possible phase should be at the very surface. This shows again that XRD is more a bulk detection technique and its result cannot be correlated with the XPS results. Other techniques should be sought to confirm the phases related to the Cr surface deposition.

3.5. Cr distribution

In order to investigate the Cr species diffusion through the porous LSM air electrode and deposition on both the LSM surface and the YSZ/LSM interface, XPS elemental analysis is employed at different locations along the LSM layer after the thermal treatment. Before the XPS analysis, the AISI 441 interconnect is removed and the porous LSM air electrode on the YSZ electrolyte is mounted in epoxy. The mounted LSM samples are carefully ground layer by layer from the top (the surface in contact with the AISI 441 interconnect) to the bottom (the YSZ/LSM interface) as shown in Fig. 1. The results are normalized to 100% by considering La, Sr, Mn, and Cr only. Along the porous LSM air electrode layer (~30 μm thick), 5 different locations are obtained for the XPS analysis (Fig. 7). The thickness of each layer is controlled by a micrometer at 8–10 μm.

Along the cross-sections of the LSM layer, from the LSM/AISI 441 interface to the locations close to the YSZ/LSM interface, the distribution of La, Sr, and Mn stays almost the same. There are some composition variations but the differences are not significant. The Cr content, however, decreases from the right to the left for all the samples. The Cr amounts at the LSM/AISI 441 interface reflect the effect of the stoichiometry. The LSM95 sample shows the lowest Cr concentration at ~7.1%; the LSM100 sample shows ~8.7%, and the LSM105 sample shows ~13.7%. Excessive A sites lead to more Cr deposition, consistent with the La replacement explanation. For all the samples, the Cr content shows a decreasing trend from the AISI 441 side to the YSZ side through the porous LSM layer (except at the YSZ/LSM interface). Compared to the Cr content of 7–14% at the LSM right location and the LSM/AISI 441 interface, the Cr content shows only 2–5% at the LSM left location (Fig. 7).

At the YSZ/LSM interface, the Cr content shows an increase for the LSM95 and LSM100 samples but a decrease for the LSM105 sample. For the LSM95 sample, the Cr content at the YSZ/LSM interface is 12.7%. For the LSM100 sample, it is 9.0%. For the LSM105 sample, the Cr content is only 2.4%, much less than those of LSM95 and LSM105. Other than Cr, the Sr content is 16.4% for the LSM95 sample, much higher than 9.6% for the LSM100 sample and 11.5% for the LSM105

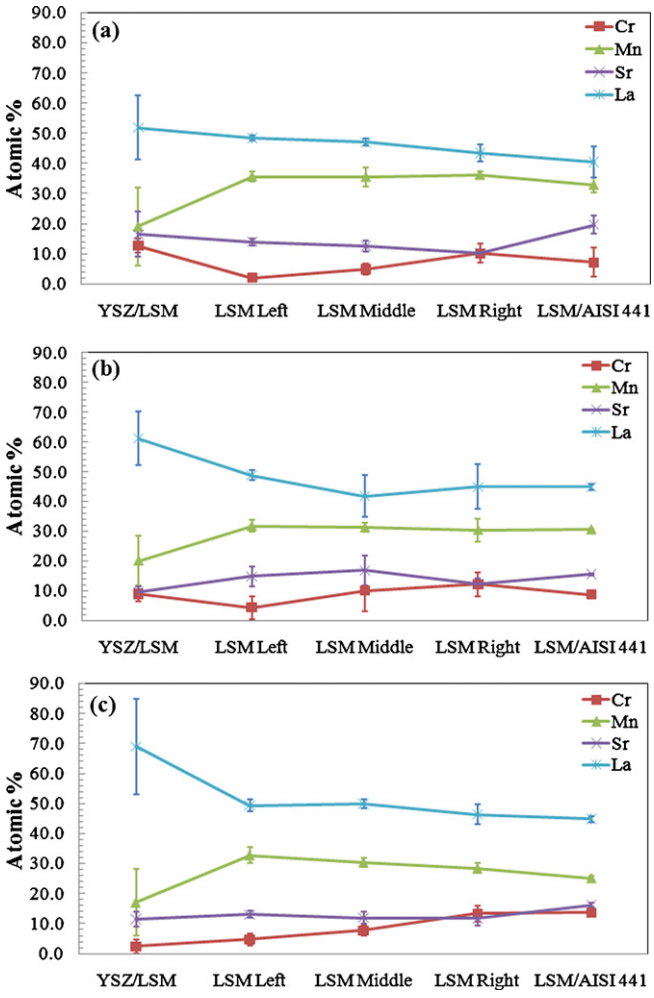

Fig. 7. Atomic concentrations along the LSM air electrode layer. The YSZ/LSM/AISI 441 samples are thermally treated in air at 800 °C for 500 h: (a) LSM95, (b) LSM100, and (c) LSM105. All the concentrations are normalized to 100% by considering La, Sr, Mn, and Cr only.

sample. The La content increases from 51.9% for LSM95, to 61.3% for LSM100, and to 69.0% for LSM105. On the other hand, the Mn content stays almost the same (17.1–20.1%), even though they are all much lower than those across the LSM layers. The different extent of Cr deposition at the YSZ/LSM interface is related to the interactions between the LSM sample and the YSZ electrolyte. As shown in Fig. 4, LSM95 and LSM100 form stronger bonds with the YSZ electrolyte. The interfacial interactions likely lead to new species formation such as $SrZrO_3$ [40]. The Cr deposition at the YSZ/LSM95 interface is accelerated by the new Sr-containing phase. From the LSM95 to the LSM105 sample (Fig. 7a–c), La shows increasing enrichment while the amount of Cr deposition decreases. This means that excessive La and likely La-containing phase (such as $La_2Zr_2O_7$ [41]) are not favorable for the Cr deposition and bond formation with the YSZ surface. Mn does not participate in these interfacial interactions but the overall depletion at the YSZ/LSM interface will compromise TPB reactivity. However, XRD cannot identify the new phases suggested by the XPS analysis. This means the amounts of these Sr-containing and La-containing phases are low and stay at the very interface.

4. Discussion

Because LSM with ABO_3 perovskite structure consists of (La,Sr)O(A-site plane) and MnO_2(B-site plane, consisted of

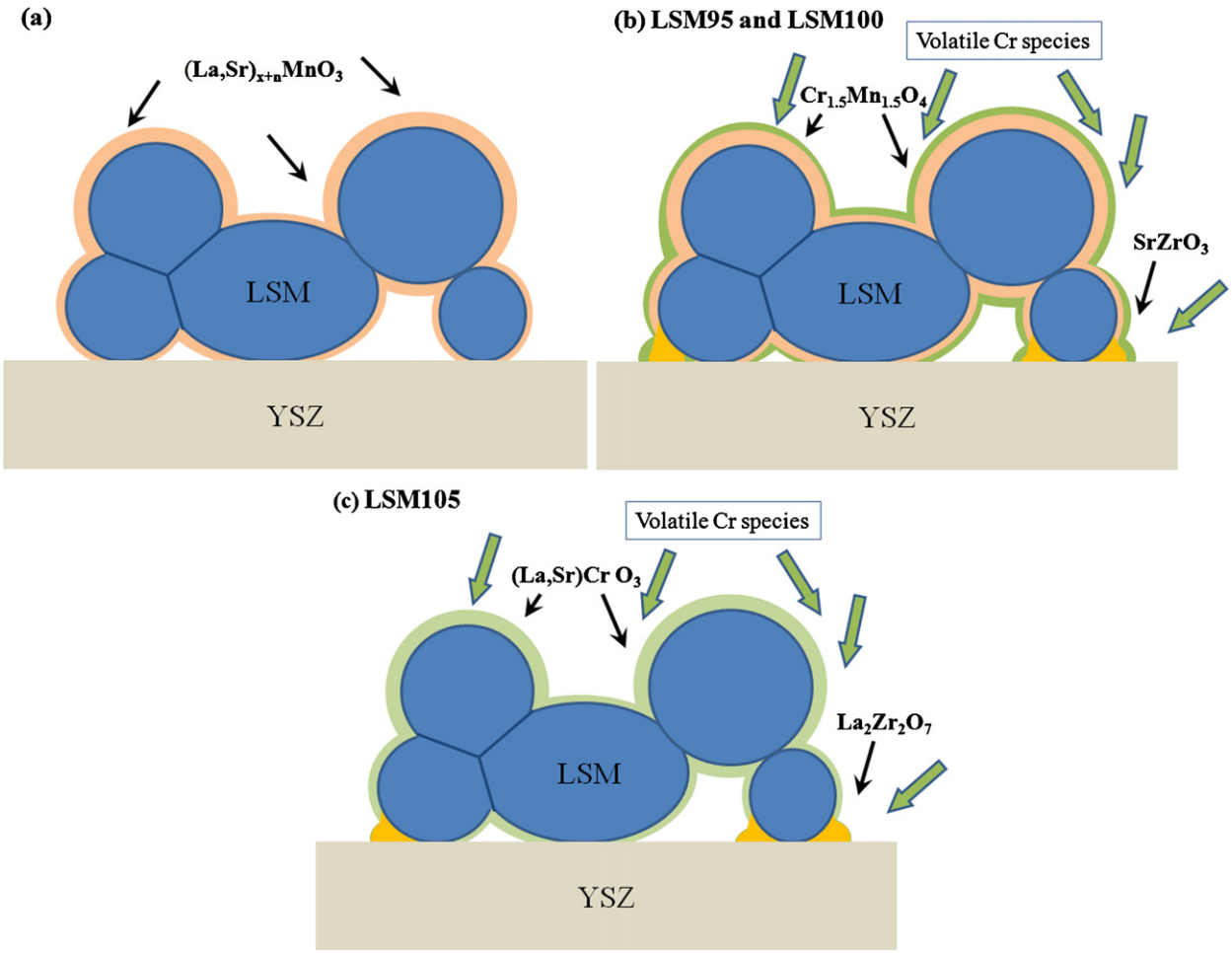

Fig. 8. Schematic of the surface and interfacial interactions of the LSM air electrode with Cr-containing species and YSZ: (a) thermally treated without Cr species, (b) LSM95 and LSM100 thermally treated with Cr species, and (c) LSM105 thermally treated with Cr species.

MnO_6octahedra) atomic layers alternatively stacked [42], the same XRD results for the as-synthesized LSM means that although the (La + Sr)/Mn ratio is slightly changed in LSM95 and LSM105, the MnO_2 layers maintain the same structure. For the as-sintered and the bi-layer samples (without Cr deposition) after the thermal treatment, the surface segregation of La and Sr fundamentally changes the (La + Sr)/Mn ratio. It is highly likely that the LSM surface cannot maintain the perovskite structure and the composition segregation occurs more easily. This La and Sr surface enrichment is mainly caused by their larger sizes. For the tri-layer samples, the Cr deposition inhibits the surface segregation of La for all the samples since it has a tendency to occupy the La sites. However, Cr can only inhibit the Sr surface segregation for the LSM100 and LSM105 samples. For the LSM95 sample, this inhibition is less effective, likely because of fewer A site species in the composition design. The $SrMn_3O_{6-x}$ phase identified in the LSM95 sample means that in the Mn excessive situation, Sr interacts with the excessive Mn first instead of waiting for the diffusing Cr species to become available.

The presence of Cr across the LSM layer indicates that Cr diffuses from the AISI 441 interconnect into the LSM air electrode layer, which in turn changes the surface structure of the LSM. The Cr-containing phase forms a very thin surface layer on the LSM since the microstructures do not show visible morphological changes and the XRD pattern shows very weak detectable peaks of the new phases. The interaction is schematically shown in Fig. 8. First of all, La and Sr surface segregation occurs (indicated in Fig. 8a by thin arrows). Then, Cr species deposit on the La–Sr enriched LSM surface, forming $Mn_{1.5}Cr_{1.5}O_4$ for the LSM95 and LSM100 samples and (La,Sr)CrO_3 for the LSM105 sample (indicated in Fig. 8b by thick arrows). The reaction equations can be expressed as:

$$(La_{0.8}\,Sr_{0.2})_xMnO_3 \xrightarrow{\text{La,Sr segregation}} (La,Sr)_{x+n}MnO_3 \quad (\text{surface}) \tag{3}$$

LSM95 and LSM100:

$$(La,Sr)_{x+n}MnO_3(\text{surface}) \xrightarrow{CrO_3} (La,Sr)_{x+n}Mn_{1-m}O_3 + \frac{2}{3}mCr_{1.5}Mn_{1.5}O_4 \quad (\text{surface}) \tag{4}$$

LSM105:

$$(La,Sr)_{x+n}MnO_3(\text{surface}) \xrightarrow{CrO_3} (La,Sr)_{x+n-m}MnO_3 + m(La,Sr)CrO_3 \quad (\text{surface}) \tag{5}$$

At the same time, Cr also diffuses to the YSZ/LSM interface.

For the LSM95 sample, excessive Mn in the initial LSM95 is beneficial for forming a good bonding between the YSZ and the LSM and the interaction leads to a significant change of the microstructure (Fig. 4b). Cr shows significant accumulation at the interface. Sr shows a higher content compared with the other two samples. At the YSZ/LSM95 interface, $SrZrO_3$may be the phase that enhances bonding and Cr accumulation. For the LSM100 sample, such interactions subdue but still exist. For the LSM105 sample, a large amount of La is present at the YSZ/LSM interface and the Cr content is much lower than those of the LSM95 and

LSM100 samples. The deficiency of Mn in the LSM105 sample leads to the $La_2Zr_2O_7$ formation and the poor interfacial bonding. Furthermore, $La_2Zr_2O_7$ at the YSZ/LSM105 interface inhibits the Cr deposition.

As seen, LSM is highly unstable on the very surface, Sr and La surface segregation and Cr deposition on the LSM surface changes the surface chemistry, the bonding between the YSZ and the LSM, and compromises the activity for oxygen reduction. These interactions can impose serious constraints on the performance and the long term stability of SOFCs/SOECs. Compared with the effects of Cr species deposition on the LSM surface, La and Sr surface segregation and the subsequent impact on the YSZ/LSM bonding and the reaction with the TPBs should be more carefully considered.

5. Conclusions

In this study, YSZ/LSM/AISI 441 samples with different LSM stoichiometries are thermally treated to study the LSM composition effect on the interfacial interactions. All the LSM samples ($(La_{0.8}Sr_{0.2})_xMnO_3$, $x = 0.95$, 1, and 1.05) show Sr and La enrichment and Mn deficiency after being thermally treated in dry air at 800 °C for 500 h. Cr surface deposition inhibits the surface segregation of La and Sr for the LSM100 and LSM105 samples. For the LSM95 sample, the Sr surface segregation is accelerated by the Cr deposition. $SrMn_3O_{6-x}$ is identified for LSM95 and $Cr_{1.5}Mn_{1.5}O_4$ is identified for both LSM95 and LSM100. Cr deposition decreases with increasing distance from the AISI 441 interconnect but increases again at the YSZ/LSM interface. The YSZ/LSM95 interface shows strong bonding; the XPS analysis shows higher Sr concentration and Cr deposition. The YSZ/LSM105 interface shows poor bonding; the XPS analysis shows higher La concentration and less Cr deposition. The fundamental mechanisms for these processes are proposed.

Acknowledgements

Financial support from Office of Naval Research under award number N00014-11-1-0266 is sincerely acknowledged. We thank ATI Allegheny Ludlum, Brackenridge, PA for providing the AISI 441 alloy sample and Tyler Corley for his valuable assistance in sample preparation.

References

[1] N.Q. Minh, J. Am. Ceram. Soc. 76 (1993) 563–588.
[2] N.Q. Minh, Solid State Ionics 174 (2004) 271–277.
[3] S.P.S. Badwal, K. Foger, Ceram. Int. 22 (1996) 257–265.
[4] S.H. Jensen, P.H. Larsen, M. Mogensen, Int. J. Hydrogen Energy 32 (2007) 3253–3257.
[5] M. Ni, M.K.H. Leung, D.Y.C. Leung, Int. J. Hydrogen Energy 33 (2008) 2337–2354.
[6] B.C.H. Steele, Solid State Ionics 134 (2000) 3–20.
[7] D.J.L. Brett, A. Atkinson, N.P. Brandon, S.J. Skinner, Chem. Soc. Rev. 37 (2008) 1568–1578.
[8] Z.G. Yang, K.S. Weil, D.M. Paxton, J.W. Stevenson, J. Electrochem. Soc. 150 (2003) A1188–A1201.
[9] W.Z. Zhu, S.C. Deevi, Mater. Sci. Eng. A 348 (2003) 227–243.
[10] J.W. Fergus, Mater. Sci. Eng. A 397 (2005) 271–283.
[11] Z.G. Yang, Int. Mater. Rev. 53 (2008) 39–54.
[12] J.W. Wu, X.B. Liu, J. Mater. Sci. Technol. 26 (2010) 293–305.
[13] J.W. Fergus, Int. J. Hydrogen Energy 32 (2007) 3664–3671.
[14] S. Taniguchi, M. Kadowaki, H. Kawamura, T. Yasuo, Y. Akiyama, Y. Miyake, T. Saitoh, J. Power Sources 55 (1995) 73–79.
[15] S.P.S. Badwal, R. Deller, K. Foger, Y. Ramprakash, J.P. Zhang, Solid State Ionics 99 (1997) 297–310.
[16] J.E. O'Brien, C.M. Stoots, J.S. Herring, J.J. Hartvigsen, Nucl. Technol. 158 (2007) 118–131.
[17] J.R. Mawdsley, J.D. Carter, A.J. Kropf, B. Yildiz, V.A. Maroni, Int. J. Hydrogen Energy 34 (2009) 4198–4207.
[18] K. Hilpert, D. Das, M. Miller, D.H. Peck, R. Weiss, J. Electrochem. Soc. 143 (1996) 3642–3647.
[19] E.J. Opila, D.L. Myers, N.S. Jacobson, I.M.B. Nielsen, D.F. Johnson, J.K. Olminsky, M.D. Allendorf, J. Phys. Chem. A 111 (2007) 1971–1980.
[20] S.P. Jiang, S. Zhang, Y.D. Zhen, J. Electrochem. Soc. 153 (2006) A127–A134.
[21] J.J. Bentzen, J.V.T. Hogh, R. Barfod, A. Hagen, Fuel Cells 9 (2009) 823–832.
[22] E. Konysheva, J. Laatsch, E. Wessel, F. Tietz, N. Christiansen, L. Singheiser, K. Hilpert, Solid State Ionics 177 (2006) 923–930.
[23] S.P. Jiang, J.P. Zhang, L. Apateanu, K. Foger, J. Electrochem. Soc. 147 (2000) 4013–4022.
[24] S.P. Jiang, J.P. Zhang, X.G. Zheng, J. Eur. Ceram. Soc. 22 (2002) 361–373.
[25] Y. Matsuzaki, I. Yasuda, J. Electrochem. Soc. 148 (2001) A126–A131.
[26] E. Konysheva, J. Mertens, H. Penkalla, L. Singheiser, K. Hilpert, J. Electrochem. Soc. 154 (2007) B1252–B1264.
[27] T. Komatsu, R. Chiba, H. Arai, K. Sato, J. Power Sources 176 (2008) 132–137.
[28] D.J. Liu, J. Almer, T. Cruse, J. Electrochem. Soc. 157 (2010) B744–B750.
[29] A. Hammouche, E. Siebert, A. Hammou, Mater. Res. Bull. 24 (1989) 367–380.
[30] T. Jin, K. Lu, Int. J. Hydrogen Energy 36 (2011) 4440–4448.
[31] G.J. la O', R.F. Savinell, Y. Shao-Horn, J. Electrochem. Soc. 156 (2009) B771–B781.
[32] V.I. Sharma, B. Yildiz, J. Electrochem. Soc. 157 (2010) B441–B448.
[33] H. Dulli, P.A. Dowben, S.H. Liou, E.W. Plummer, Phys. Rev. B 62 (2000) 14629–14632.
[34] N. Mannella, A. Rosenhahn, A. Nambu, B.C. Sell, B.S. Mun, S.H. Yang, S. Marchesini, M. Watanabe, K. Ibrahim, S.B. Ritchey, Y. Tomioka, C.S. Fadley, J. Electron Spectrosc. Relat. Phenom. 153 (2006) 37–57.
[35] N. Caillol, M. Pijolat, E. Siebert, Appl. Surf. Sci. 253 (2007) 4641–4648.
[36] P. Decorse, G. Caboche, L.C. Dufour, Solid State Ionics 117 (1999) 161–169.
[37] F.F. Abraham, C.R. Brundle, J. Vac. Sci. Technol. 18 (1981) 506–519.
[38] J.G. Speight, Lange's Handbook of Chemistry, sixteenth ed., McGraw-Hill, NY, 2005.
[39] J.C. Vickerman, I.S. Gilmore, Surface Analysis: The Principal Techniques, second ed., Wiley, Chichester, UK, 2009.
[40] Y.L. Liu, A. Hagen, R. Barfod, M. Chen, H.J. Wang, F.W. Poulsen, P.V. Hendriksen, Solid State Ionics 180 (2009) 1298–1304.
[41] A. Mitterdorfer, L.J. Gauckler, Solid State Ionics 111 (1998) 185–218.
[42] H. Kumigashira, K. Horiba, H. Ohguchi, K. Ono, M. Oshima, N. Nakagawa, M. Lippmaa, M. Kawasaki, H. Koinuma, Appl. Phys. Lett. 82 (2003) 3430–3432.